Nanofluidic delivery implant sustains localization and maximizes efficacy of intratumoral immunotherapy

Original
Nanofluidic delivery implant sustains localization and maximizes efficacy of intratumoral immunotherapy / Liu, Hsuan-Chen; Di Trani, Nicola; Conte, Marzia; Chuong Nguyen, Dinh; Jokonya, Simbarashe; Wu, Abe; Vander Pol, Robin; Joubert, Ashley L.; Facchi, Ilaria; Wood, Anthony M.; Ho, Jeremy; Pesaresi, Federica; Cauda, Valentina; Chen, Shu-Hsia; Liu, Xuewu; Stayton, Patrick S.; Ying Xuan Chua, Corrine; Grattoni, Alessandro. - In: NANO TODAY. - ISSN 1748-0132. - ELETTRONICO. - 56:(2024), pp. 1-11. [10.1016/j.nantod.2024.102258]

Publisher:
Elsevier

Published
DOI:10.1016/j.nantod.2024.102258

Nano Today 56 (2024) 102258

Contents lists available at ScienceDirect

Nano Today

journal homepage: www.elsevier.com/locate/nanotoday

Nanofluidic delivery implant sustains localization and maximizes efficacy of intratumoral immunotherapy

Hsuan-Chen Liu [a,1], Nicola Di Trani [a,1], Marzia Conte [a,b], Dinh Chuong Nguyen [c], Simbarashe Jokonya [c], Abe Wu [c], Robin Vander Pol [a], Ashley L. Joubert [a], Ilaria Facchi [a], Anthony M. Wood [a], Jeremy Ho [a], Federica Pesaresi [a], Valentina Cauda [b], Shu-Hsia Chen [d,e], Xuewu Liu [a], Patrick S. Stayton [c], Corrine Ying Xuan Chua [a,*], Alessandro Grattoni [a,f,g,**]

[a] *Department of Nanomedicine, Houston Methodist Research Institute, Houston, TX 77030, USA*
[b] *Department of Applied Science and Technology, Politecnico di Torino, Corso Duca degli Abruzzi 24, Torino 10129, Italy*
[c] *Department of Bioengineering and Molecular Engineering & Sciences Institute, University of Washington, Seattle, WA, USA*
[d] *Center for Immunotherapy Research, Houston Methodist Research Institute, Houston, Texas, USA*
[e] *ImmunoMonitoring Core, Houston Methodist Research Institute, Houston, Texas, USA*
[f] *Department of Surgery, Houston Methodist Research Institute, Houston, TX 77030, USA*
[g] *Department of Radiation Oncology, Houston Methodist Research Institute, Houston, TX 77030, USA*

ARTICLE INFO

Keywords:
Intratumoral immunotherapy
Drug delivery
Controlled release
Nanofluidic implant
Immune checkpoint inhibitors
STING agonist
Toll-like receptor agonist

ABSTRACT

Intratumoral immunotherapy holds promise for improving cancer treatment efficacy. However, rapid clearance from the tumor upon bolus volume injections limits efficacy and impedes assessment of dose-dependent effects on the tumor immune microenvironment (TIME). To this end, we developed a drug-agnostic nanofluidic implant to deliver immunotherapy within the tumor, providing a mechanism for sustained and controlled intratumoral dosing. Diffusive drug elution from the implant reservoir is controlled by a nanofluidic membrane, which abrogates rapid drug elimination from the tumor and maximizes immunotherapy localization. Here we first achieve *in vitro* sustained release of agonist CD40 monoclonal antibody (mAb), anti-programmed death ligand-1 (PDL1) mAb, and immune-cell targeted polymeric prodrugs of Resiquimod (toll-like receptor 7/8,TLR 7/8) and a small molecule STING agonist. We then demonstrated *in vivo* sustained intratumoral drug localization of agonist CD40 Ab and anti-PDL1 Ab in the 4T1 murine model of triple-negative breast cancer (TNBC). Further, we show highly effective anti-tumor efficacy with radiation therapy and sustained intratumoral co-delivery of agonist CD40 Ab and anti-PDL1 Ab in the EMT6 TNBC murine model. Finally, we demonstrate the versatility of this implant by showing that sustained intratumoral delivery of the STING or Resiquimod polymeric prodrugs strongly inhibits 4T1 tumor growth. Collectively, these results support our nanofluidic system as a therapeutic platform technology to investigate sustained intratumoral dosing of immunotherapy.

Introduction

Immunotherapy has transformed the field of oncology with the potential for treating cancers by harnessing the immune defense mechanism. Although promising, immunotherapy has shown variable responses across different cancers, in part due to delivery failure rather than drug ineffectiveness [1]. Ultimately, the efficacy of immunotherapy hinges on modulating the tumor immune microenvironment (TIME) to be responsive to treatment [2,3]. Immunotherapeutic agents are systemically administered, and only a small amount penetrates the tumor, which contains therapeutically relevant local immune infiltrates [4,5]. As such, the effect of systemically delivered immunotherapy on the TIME is hard to discern.

In view of this, intratumoral immunotherapy is clinically investigated as an alternative delivery route to enhance drug localization within the tumor and minimize off-target exposure [6–9]. Intratumoral

---

* Corresponding author.
** Corresponding author at: Department of Nanomedicine, Houston Methodist Research Institute, Houston, TX 77030, USA.
E-mail addresses: ychua@houstonmethodist.org (C.Y.X. Chua), agrattoni@houstonmethodist.org (A. Grattoni).
[1] These authors equally contributed to this work.

https://doi.org/10.1016/j.nantod.2024.102258
Received 4 October 2023; Received in revised form 21 March 2024; Accepted 31 March 2024

immunotherapy is predicated on the premise that acting locally on existing tumor immune infiltrates enables priming of a global, amplified antitumor immune response [10]. Currently, intratumoral immunotherapy is delivered through direct bolus injections, which bypasses biological barriers to drug uptake [11]. However, bolus injections rapidly disperse out of the tumor, invariably affecting local drug concentration and impact on the TIME, thus confounding the understanding of dose versus effect [12,13]. To this end, an intratumoral delivery mechanism that permits sustained and controlled immunotherapy release at known doses while avoiding rapid leakage from the tumor could provide insights into optimal therapeutic regimens [14].

Polymeric drug eluting systems such as in situ forming gels and micro- and nanoparticles are actively explored intratumorally [12,14]. Although these systems provide prolonged drug delivery, their inconsistent release rates, burst and decay release profiles and terminal dose dumping lower the efficacy and narrow the therapeutic window of immunotherapeutics. To achieve better control of drug exposure within the tumor, we developed a drug-agnostic intratumoral delivery platform capable of sustained and constant immunotherapy elution via a nanofluidic membrane [15–17]. In contrast with degradable depot systems, which carry limited amounts of drugs that are both surface-bound and dispersed often irregularly within the polymer matrix, our implant houses drugs in powder form. This permits the adoption of various agents alone or in combination without requiring complex formulation development. Moreover, drug-loading efficiency is significantly enhanced, which is advantageous for intratumoral delivery where a small implant volume is required for minimally-invasive delivery. In our platform, drug release is controlled by electrostatic hindrance within the nanochannels and occurs through diffusive transport [18–21], which avoids immediate clearance from the tumor and enhances local retention and dissemination. This controlled method of delivery addresses the issue of inconsistent and early and/or late-stage burst drug exposure in the tumor, which confounds the understanding and optimization of drug dose versus anti-tumor activity. This mechanism also allows the release kinetics to be modulated and tuned in relation to the immune-therapeutic size and diffusion properties.

Here we explore intratumoral sustained release through our nanofluidic platform using different types of immunotherapeutic agents, namely agonist CD40 monoclonal antibody (mAb), anti-programmed death ligand-1 (PDL1) mAb, a polymeric prodrug of Stimulator of Interferon Genes (STING) agonist, and a polymeric prodrug of Toll-Like Receptor 7/8 (TLR 7/8) agonist (resiquimod, R848). STING agonists stimulate the production of type I interferon (IFN) and inflammatory cytokines, and subsequently activate dendritic cells (DCs) and enhance presentation of antigens to CD8+ T cells [22]. Similarly, R848 binds to TLR7/8 and exerts its antitumor effects through activation and maturation of DCs and stimulation of inflammatory cytokine production [23]. These polymeric prodrugs are also targeted to CD206-expressing immune cells (e.g. tumor associated macrophages and dendritic cells) via a mannosylated ligand that is incorporated into the polymer structure. CD40 mAb mediates antitumor activities through DCs, macrophages and T cell activation [24]. Immune checkpoint blockade through anti-PDL1 mAb induces T cell reinvigoration to reactivate cytotoxic T cell activity [25]. We demonstrate the application of our platform for intratumoral immunotherapy in EMT6 and 4T1 murine models of triple negative breast cancer (TNBC). Overall, our technology represents a clinically relevant drug-agnostic therapeutic platform for the analysis of sustained intratumoral immunotherapy dosing.

Materials and methods

Materials

All chemicals were purchased from Sigma-Aldrich unless otherwise stated. The STING agonist “STING Agonist-3” (CAS 2138299–29–1) was purchased from MedChemExpress. The TLR 7/8a agonist Resiquimod (R848) was purchased from Toronto Research Chemicals. RAFT chain transfer agent 4-(((ethylthio)carbonothioyl)thio)-4-cyanopentanoic acid (ECT) and the monomer mannose ethyl methacrylate (ManEMA) were purchased from Omm Scientific. The rhodamine monomer, methacryloylethyl thiocarbamoyl rhodamine B (RhMA) was purchased from PolySciences Inc. The initiator 2,2′-azobis(4-methoxy-2,4-dimethylvaleronitrile) (also known as V70) was purchased from Wako Fujifilm. 4-nitrophenol chloroformate (PNP-Cl) was purchased from Chem-Impex International Inc. Dimethylformamide (DMF), tetrahydrofuran (THF), dichloromethane (DCM) and chloroform were purchased from Fisher. Argon gas was purchased from Linde Gas & Equipment Inc. All reagents mentioned above were used as received.

Membrane fabrication

The membranes in this study were fabricated starting from a 4-inch silicon-on-insulator (SOI) wafer with a 10 μm device layer, 1 μm middle oxide layer and 400 μm handle layer (Ultrasil Corporation, Hayward, CA). The fabrication steps are summarized in Fig. 1. First, 500 nm of silicon dioxide SiO2 were grown on the wafer by wet thermal oxidation (1050 °C) as a photolithography mask (Fig. 1A). Using a standard photolithographic process, nanochannels array templates (500 nm x 6 μm) were patterned on the oxide surface using a contact aligner (KARL SUSS MA6) and NR9–500 P photoresist (Futurrex, Franklin, NJ). The template pattern was transferred into the oxide layer by fluorine based (5:1 ratio of CHF3:CF4) reactive ion etch (RIE), and then etched through the 10 μm device layer by deep silicon etching (DSE) on an ICP deep silicon etcher (PlasmaTherm, Versalline)(Fig. 1B). A custom developed DSE nanoetching recipe was used to get smooth sidewalls. Each cycle of the recipe incudes polymer deposition for 2 s (C4F8 150 sccm, Ar 30 sccm, pressure 25 mTorr, and Bias RF 10 V), polymer removal from bottom of trench for 1.5 s (SF6 50, Ar 30 sccm, pressure 20 mTorr, and Bias RF 300 V), and silicon etch for 0.75 s (SF6 50, Ar 30 sccm, pressure 25 mTorr, and Bias RF 10 V). ICP RF power was 5000 W for all the steps. The microchannels (μCh, 150 μm diameter) and device release outer ring (1.2 mm diameter and 7.5 μm width) were patterned on the backside using double-side alignment on a contact aligner (KARL SUSS MA6) and SPR 220–4.5 photoresist. The patterns were etched into the 400 μm handle layer via DSE on an ICP deep silicon etcher (PlasmaTherm, Versalline) for about 500 cycles (Fig. 1C). This step completely etched through the handle layer and stopped on the middle oxide layer for the μCH pattern. Simultaneously the release ring was etched to about 250 μm depth. The backside etching used a fast DSE recipe, which includes polymer deposition for 2.5 s (C4F8 75 sccm, Ar 30 sccm, pressure 25 mTorr, and Bias RF 10 V), polymer removal from bottom of trench for 1.5 s (SF6 150 sccm, Ar 30 sccm, pressure 20 mTorr, and Bias RF 250 V), and silicon etch for 3 s (SF6 300 sccm, Ar 30 sccm, pressure 25 mTorr, and Bias RF 10 V). ICP RF power was 4000 W for these steps. The accumulated polymer on sidewall during DSE was cleaned in solvent based solution. The wafer was then Piranha cleaned and dipped in BOE solution for 10 minutes to remove the 1 μm middle SiO2 layer (Fig. 1D). A wet thermal oxidation was then performed at 1050 °C to grow a high temperature SiO2 oxide that shrinks the nanochannel size to the desired size. Using a standard photolithographic technique, a 250 μm wide top open ring was patterned on the device layer (nanochannel side) using a contact aligner (KARL SUSS MA6) and SPR 220–4.5 photoresist. A 4-step etching was performed to reach the release ring etched on the handle layer (Fig. 1F). Briefly, RIE was used to etched through the top oxide layer, DSE to etch through 10 μm of device layer, RIE to etch the 1 μm of middle oxide layer and finally DSE to etch through the remaining 150 μm of silicon and reach the release ring patterned on the handle layer. The sidewall polymer and residual photoresist was then cleaned. The entire wafer was successively coated with a 50 nm silicon carbide (SiC) layer via plasma-enhanced chemical vapor deposition (PECVD, Fig. 1G). Fig. 1E shows a close up of the nanochannels to highlight the different layers: silicon structure coated with SiO2 and SiC. Each

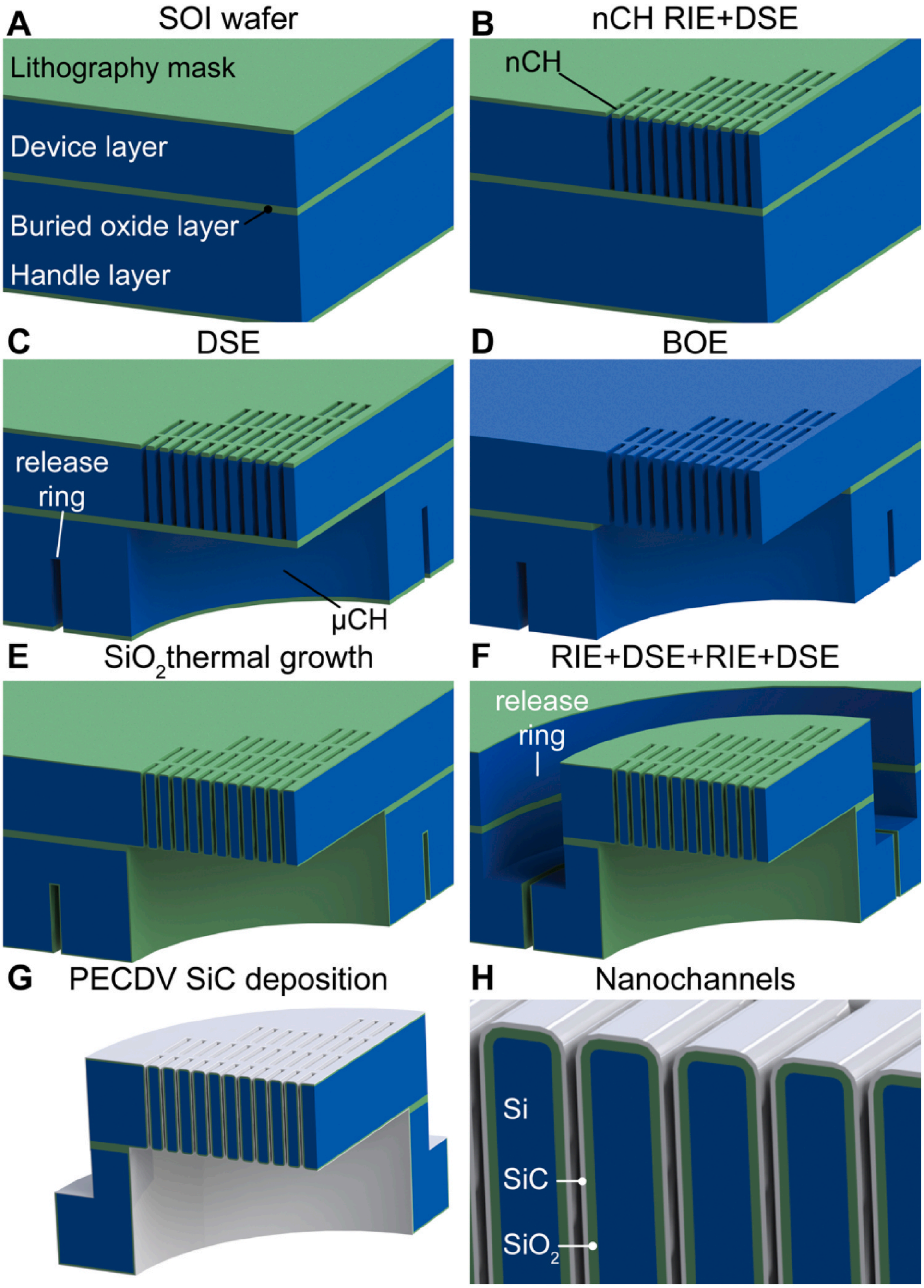

Fig. 1. Fabrication process schematics. A) Silicon on insulator (SOI) wafer with lithography mask. B) Nanochannel (nCH) patterning, reactive ion etching (RIE) for the oxide and deep reactive ion etching (DRIE) for the silicon. C) DRIE for microchannels (μCH) and release ring. D) Buffered oxide etch (BOE) for SiO2 removal. E) SiO2 thermal oxidation growth. F) Release ring 4 step etch. G) Silicon carbide (SiC) deposition. H) Nanochannels highlight with different layers.

membrane features 7 microchannels, where each one is connected to a 19 rows by 96 column array of 1400 identical slit nanochannels. The 4 in. wafer contains 1044 membranes, connected to the wafer by a micrometric latching feature that can be release by gentle pressure.

NDES assembly

A 3.5 mm-long stainless-steel hollow tube is used as a drug reservoir. The fabricated membrane was settled on top of the hollow tube, glued with biocompatible thermal epoxy (EPO-TEK 354-T) and cured at 60 °C overnight. This adhesive has high bonding strength, is bioinert, suitable for long-term implantable applications, thermally and hygroscopically stable, and withstands sterilization via autoclaving. Lyophilized drugs are loaded in the drug reservoir in powder from by using a custom-made funnel that allows for powder insertion and compacting inside the device. The 2 μl reservoir can contain up to 1.5 mg of powdered antibody.

The end sealed with fast-cure silicone adhesive that was dried at 4 °C overnight. To reinforce sealing integrity and prevent drug leakage from NDES during the implantation procedure, ultraviolet (UV) epoxy (Epotek OG116–31) was employed over the silicone cap and cured with a long wavelength UV gun (365 nm). The assembled NDES were primed for drug release in 1 mL of phosphate-buffered saline (PBS) solution under vacuum.

Antibodies

CD40 (FGK4.5, BE0016) and PD-L1 (10 F.9G2, BE0101) monoclonal antibodies were acquired from Bio X Cell. To produce lyophilized antibodies, we followed the procedure described in the previous publication [26,27]. Briefly, for in vivo design, CD40 and PD-L1 monoclonal antibodies were concentrated with Amicon Ultracel-30k and labeled with Alexa Fluor 647 (A37573, Invitrogen™) and Alexa Fluor 790 (A37569, Invitrogen™), respectively. The stock solution of CD40-AF647 and PD-L1-AF790 were mixed together with 1:1 ratio. The mixture of antibodies was added D-(+)-trehalose dihydrate (90210, Millipore-Sigma) and frozen at –80 C and lyophilized with FreeZone freeze dryer system (LABCONCO Freezone 4.5) for 48 hours. For the in vitro design experiment, CD40 and PD-L1 were lyophilized without Alexa flour labeling separately.

Synthesis of poly-STING

The STING Agonist prodrug was synthesized according to protocols detailed in the Supplementary Information (Scheme S1, Compound 8a). For the RAFT polymerization of the mannosylated polymeric prodrug poly-STING, ManEMA (200 mg, 0.68 mmol, 35.7 eq) and the STING agonist prodrug monomer (55.9 mg, 0.044 mmol, 2.2 eq), were all dissolved in DMSO-d6 (0.34 mL) in a 5 mL oven-dried pear-shaped flask. Trioxane (15 mg) was added as an internal standard for monomer conversion calculations. Next, a stock solution (20.2 mg/mL in DMSO-d6) of the RAFT chain transfer agent ECT (0.25 mL, 5.05 mg, 0.019 mmol, 1 eq) was added. Thereafter, a stock solution of V70 (17.7 mg/mL in anhydrous DMF) was prepared and quickly added to the solution (0.05 mL, 0.88 mg, 0.0029 mmol, 0.15 eq). After taking a small aliquot (0.02 mL) for NMR conversion analysis, the reaction vessel was sealed with a septum and purged with argon gas for 30 minutes. The flask was then placed into an oil bath set to 42 C, and allowed to react for 22 hours. Upon completion, the reaction mixture was dialyzed against DMSO (500 mL) for 3 days using a SnakeSkin 3.5 kDa MWCO regenerated cellulose membrane, changing the DMSO twice daily. The reaction mixture was then dialyzed against ice-cold water (4 C, 4000 mL) in a cold room for 2 days to remove DMSO, changing water twice daily. The dialysate was then lyophilized for 3 days to yield 188 mg (85% gravimetric conversion) of poly-STING.

For the synthesis of rhodamine-labelled poly-STING (Rh-poly-STING), 3.8 mg of RhMA (0.0055 mmol, 0.38 eq) was added to the following: 0.48 mL DMSO-d6, 150 mg of ManEMA (0.51 mmol, 35.3 eq), 42.4 mg of STING agonist prodrug monomer (0.038 mmol, 2.3 eq), 3.82 mg of ECT (0.015 mmol, 1 eq) and 0.67 mg of V70 (0.0022 mmol, 0.15 eq). Following the addition of RhMA, RAFT polymerization and purification was performed as for the unlabeled polymer above. The final polymer compositions were verified by proton-NMR, with Mw characterized by GPC. The NMR and GPC polymer characterizations are provided in supplementary information (Table S1, Figure S3 and S7).

Synthesis of poly-R848

The prodrug monomer of the TLR 7/8a agonist Resiquimod (R848) was synthesized according to protocols detailed in the Supplementary Information (Scheme S1, Compound 8b). For the RAFT polymerization of the mannosylated polymeric prodrug poly-R848, ManEMA (308 mg, 1.05 mmol, 34.4 eq), the Resiquimod prodrug monomer (160 mg, 0.171 mmol, 5.6 eq), and ECT (8.1 mg, 0.031 mmol, 1 eq) were all dissolved in DMSO-d6 (1.12 mL) in a 5 mL oven-dried round-bottom flask. Trioxane (15 mg) was added as an internal standard for monomer conversion calculations. Thereafter, a stock solution of V70 (37.8 mg/mL in anhydrous DMF) was prepared and quickly added to the solution (0.025 mL, 0.95 mg, 0.0031 mmol, 0.1 eq). After taking a small aliquot (0.02 mL) for NMR conversion analysis, the reaction vessel was sealed with a septum and purged with argon gas for 30 minutes. The flask was then placed into an oil bath set to 35 C, and allowed to react for 16 hours. Upon completion, the reaction mixture was dialyzed against DMSO (500 mL) for 3 days using a SnakeSkin 3.5 kDa MWCO regenerated cellulose membrane, changing the DMSO twice daily. The reaction mixture was then dialyzed against ice-cold water (4 C, 4000 mL) in a cold room for 2 days to remove DMSO, changing water twice daily. The polymer was further purified by PD-10 desalting column. The solution was then lyophilized for 3 days to yield 226.8 mg (49% gravimetric conversion) of poly-Resiquimod/poly-R848.

For the synthesis of rhodamine-labelled poly-R848 (Rh-poly-R848), 7 mg of RhMA (0.0105 mmol, 1 eq) was added to the following: 0.45 mL DMSO-d6, 105 mg of ManEMA (0.36 mmol, 34.4 eq), 55 mg of the Resiquimod prodrug monomer (0.059 mmol, 5.6 eq), 2.76 mg of ECT (0.0104 mmol, 1 eq) and 0.49 mg of V70 (0.00104 mmol, 0.1 eq). Following the addition of RhMA, the RAFT polymerization and purification was performed as for the unlabeled polymer above. The final polymer compositions were verified by proton-NMR, with Mw characterized by GPC. The NMR and GPC polymer characterizations are provided in supplementary information (Table S1, Figure S6 and S7).

In vitro release

NDES were assembled as described in section 2.3 and loaded with the immunotherapeutic agents of interest (CD40, PD-L1, Poly-Resiquimod, Poly-STING) separately. The primed NDES were immersed in 3 mL of PBS solution in cuvettes for UV/Vis spectroscopy measurements. A Teflon coated stir-bar was used to maintain continuous solution homogenization. The cuvettes were positioned in a temperature controlled chamber (37 ºC) connected to a custom-built robotic carousel (Quantum Northwest, Inc) UV/Vis spectrophotometer (Cary 50; Agilent Technologies) [28]. Absorbance was measured every 5 minutes for 5–7 days, at 280 nm, 280 nm, 250 nm and 317 nm for CD40, PDL1, poly-R848 and poly-STING, respectively. The cumulative release of antibodies was calculated based on Beer-Lambert law.

Animals

Seven-week-old Balb/c mice were purchased from Taconic Biosciences (Rensselaer, NY). Animals were housed at the Houston Methodist Research Institute Comparative Medicine facility following the protocols outlined in the National Institutes of health guide for Care and Use of Laboratory Animal. All animals were monitored daily, and all studies were conducted in accordance with protocols approved by the Institutional Animal Care and Use Committee. For in vivo imaging, mice were given alfalfa-free diet to minimize background autofluorescence.

Triple negative breast cancer 4T1 (CRL02539) and murine mammary carcinoma EMT6 (CRL-2755) cell lines were obtained from American Type Culture Collection and cultured according to manufactured culture protocol. For inoculation, low passage cells were resuspended at 3×10^4 cells (4T1) or 5×10^5 cells (EMT6) in 100 µl of 3:1 mixture of PBS and Matrigel matrix. The cell mixture was injected at the fourth left mammary fat pad. Tumor volume was monitored thrice weekly. Mice received the implant when tumor volume reached about 120 mm^3 following previously described protocol.[27]

CT imaging

We used the Siemens Inveon Multi-Modality System controlled with the Inveon Acquisition Workplace (IAW) for CT imaging of the NDES in 4T1 tumor-bearing mice.

In vivo biodistribution

NDES were intratumorally implanted in 4T1 tumors using a minimally invasive trocar approach similar to brachytherapy seed insertion. Drug release from the NDES was monitored daily using an in vivo imaging system (IVIS Spectrum, Perkin Elmer). Fluorescent images were taken with excitation/emission rate at 594/650 nm for Alexa fluor 647, and 784/841 nm for Alexa fluor 790.

In vivo efficacy

Radiation-treated mice were anesthetized with inhaled isoflurane and intraperitoneal dexmedetomidine with 5 µg/g (body weight) before radiation. Radiation was administered using RS 2000 small animal irradiator (160 kV, 25 mA and 2 Gy/min mean beam rad source; Brentwood, TN). EMT6 tumor-bearing mice received 5 Gy for 3 consecutive days before NDES implantation. A rigid exposed-flank shield (Precision X-ray Inc.) and a flexible lead layer were used to shield the mice from irradiation while exposing only the tumor. Anti-sedative, atipamezole, was given to reverse dexmedetomidine anesthesia. To maintain the mice health post-radiation, subcutaneous fluid and moist chow were given daily. For the Rad + NDES combo cohort, NDES were intratumorally implanted one day after the third radiation dose.

For the bilateral EMT6 model, the mice were inoculated with 1×10^5 cells at the fourth left mammary fat pad and 5×10^4 cells at the fourth right mammary fat pad. Tumors were measured thrice a week. Animals were randomized in the experimental groups when the left ‘primary’ tumors were about 120 mm^3 and the right ‘distant’ tumors were in the range of 30–70 mm^3.

NDES containing poly-STING agonist or poly-R848 were each implanted into 4T1 tumors when their volume reached about 120 mm^3.

Statistical analysis

Statistical analysis was performed in GraphPad Prism 10.0.2. For multiple group comparisons, an analysis of variance (ANOVA) was performed. Unpaired 1-way, 2-way ANOVA and multiple comparisons were performed using Tukey corrections. $p < 0.05$ was considered significant.

Results and discussion

Miniaturized nanofluidic membrane

All wafers and membranes were visually inspected for quality of the fabrication process via optical microscopy (Fig. 2A). Subsequently, SEM images were obtained to analyze the micro- and nanoscale membrane structure. Each wafer yielded 1044 identical membranes. Fig. 2B shows the magnification of an individual membrane (backside view) and the sacrificial latching feature keeping the membrane connected to the wafer during the fabrication process. The sacrificial latches were designed to safely release the membranes from the wafer by applying gentle pressure. Fig. 2C shows an SEM image of the front side of an individual membrane at 60º inclination exposing the 7 circular areas containing the nanochannels arrays. These areas are pseudo-colored blue for clarity of visualization. The membranes were microfabricated with a tiered discoidal structure with larger and smaller diameters of 1100 and 900 µm, respectively. This design allowed for rapid and reproducible implant assembly, with the membrane fitting within one end of the cylindrical tubular drug reservoir (Fig. 2D). Each membrane was microfabricated with 1400 through slit-nanochannels arranged regular arrays (Fig. 2E). Each circular pattern of nanochannels corresponds to a microchannel on the opposite side of the wafer. Fig. 2F shows vertically etched nanoslits in a cross-section of the membranes obtained with focused ion beam milling. The uniformity of nanochannel size was assessed via imaging and nitrogen flow analysis (at 15 psi differential pressure) on 10 membranes selected from different areas of the wafer. An average size of 152 ± 10 nm was obtained using a gas flow model previously validated in our laboratory[29]. The thickness of the different layers on the membrane surface were quantified via ellipsometry. Specifically, ~250 nm of SiO_2 were thermally grown to accurately control the slit-nanochannel dimension. An outer SiC layer (~50 nm) was deposited on top of SiO_2 to provide biocompatibility and bioinertness for in *vivo* applications.

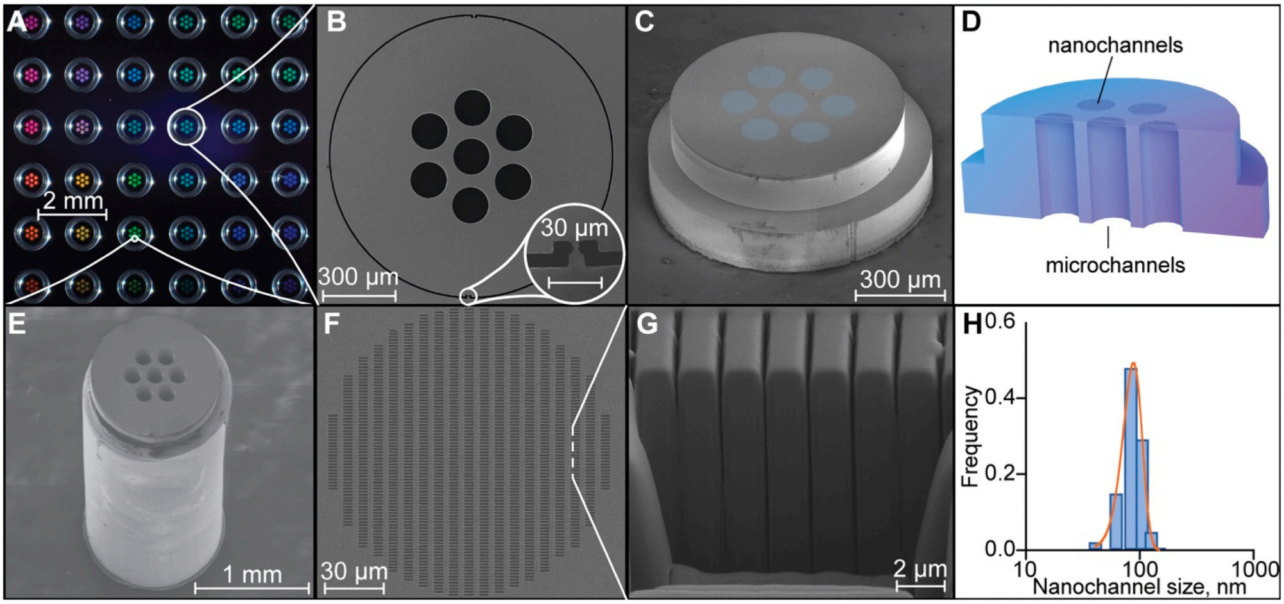

Fig. 2. Nanofluidic membrane. A) Optical microscope image of a silicon wafer with an array of nanofluidic membranes. B) SEM image of the backside view of the membrane showing the 7 microchannel honeycomb etched within the wafer handle layer; the inset shows the membrane release mechanism. C) SEM of a nanofluidic membrane at 60º tilt showing the 7 circular areas containing the arrays of nanochannels (image colored in blue for clarity) on the membrane front side. D) Rendering of a cross section of the membrane showing the microchannels and nanochannels. E) SEM image of the nanochannel membrane positioned on top of the stainless steel drug reservoir. F) Top front side view of the nanochannel array. G) FIB cross-section along the nanochannel length, perpendicular to the membrane surface. H) Nanochannel size distribution.

In vitro drug release

To evaluate the ability to control the release of immunomodulatory molecules, the *in vitro* drug release from the NDES was tested using agonist CD40 Ab, anti-PDL1 Ab as well as mannose-targeted polymeric prodrugs of Resiquimod (Poly-R848) and STING agonist (Poly-STING).

Resiquimod (R848) is a well-known agonist for the Toll-Like Receptor 7/8a [30] (TLR 7/8a) currently under investigation as a cancer immunotherapeutic.[31] The STING agonist in this work ("STING-3" in Fig. 3c) was derived from the established diamidobenzimidazole (diABZI) STING agonist family, which shows systemic activity in murine tumor models.[32] The derivative compound carries a hydroxyl group amenable to our functionalization as described hereafter. The small-molecule adjuvants are formulated as a cathepsin B-labile prodrug monomers, and copolymerized with mannose ethyl methacrylate to yield polymeric mannose-targeted adjuvant prodrugs ("drugamers"). The polymeric design imparts superior pharmacokinetics, while copolymerization with mannose targets antigen presenting cells such as macrophages and dendritic cells through endocytosis via the mannose receptor [33]. We have previously demonstrated the enhanced targeting properties of polymerized drugs with a variety of copolymer [33–35] and micellar [36,37] drug carriers, demonstrating CD206-dependent uptake in macrophage [33–35] and dendritic cells [36,37] across several types of tissues, organs and tumors. This targeting approach is also demonstrated in published work from other groups [38,39].

The cathepsin B-labile monomer design allows for adjuvant release in the maturing endosome, imparting bioavailability within cells that uptake the drugamers. Specifically, R848 and STING were formulated into cathepsin-laile prodrug monomers, and copolymerized with Mannose Ethyl Methacrylate (ManEMA) using RAFT polymerization to produce the linear polymeric prodrugs poly-R848 and poly-STING (Fig. 3c). poly-STING has a molecular weight of 12 kDa with 35 mannose/chain and 1–2 prodrug/chain, and poly-R848 has a molecular weight of 15 kDa with 34 mannose/chain and 5–6 prodrug/chain (details in Table S1 in the Supplementary Information).

Given the small volume of the implant drug reservoir (2 μL), all drugs were individually loaded in the implant in lyophilized powder form in absence of excipients. Drug elution from implants was quantified within UV-cuvettes containing PBS as sink solution (Fig. 3A). A custom robotic UV-Vis spectrophotometer allowed for measurement of absorbance at high sampling frequency without fluid manipulation. All molecules showed sustained steady delivery over the course of analysis at the rates of 6.19 ± 0.21 μg/day (agonist CD40 Ab), 3.62 ± 0.25 μg/day (anti-PDL1 Ab), 14.52 ± 0.44 μg/day (Poly-R848), 25.67 ± 1.39 μg/day (poly-STING, full membrane), 7.00 ± 0.21 μg/day (poly-STING, 3/8 membrane). No signs of release inflection were observed, with cumulative release profiles stabilizing after 24–48 hours from initiation of release. Antibody release from the implants is achieved via a counter diffusion of sink fluid into the implant, which allows for the solubilization of a portion of the drug. This generates a saturated drug solution

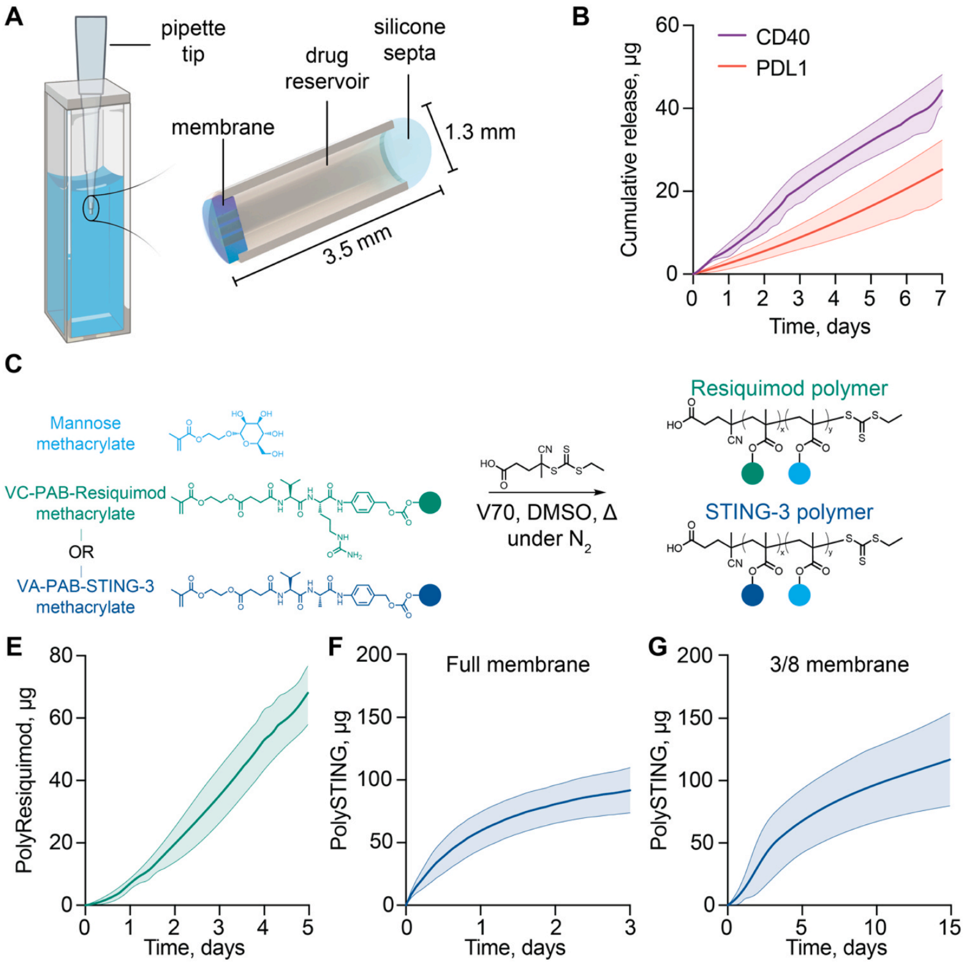

Fig. 3. *In vitro* release with nanofluidic drug eluting seed (NDES). A) Schematic of the experimental setup for in-vitro drug release. The NDES is positioned inside a cuvette, suspended in solution via a pipette tip. B) Cumulative release of agonist CD40 Ab and anti-PDL1 Ab. C) Structure and polymerization schematic for poly-R848 and poly-STING. E) Cumulative release of Rh-poly-R848 from the NDES. F) Cumulative release of Rh-poly-STING from the NDES with full membrane. G) Cumulative release of Rh-poly-STING from the NDES with 3/8 of membrane.

within the drug reservoir and establishes a stable concentration gradient across the membrane. Drug diffusion in nanochannels is influenced by molecules properties such as size, charge and hydrophilicity as well as nanochannels size and surface charge. The diffusive release of molecules is also determined by nanochannel size and number and allows for a quasi-constant drug release until drug depletion [40–43]. The release of the two polymeric prodrugs follows the same principle. These polymers do have different shape and hydrodynamic parameters compared to globular proteins. The versatility of the NDES is thus demonstrated with these two interesting immune therapeutics, where the ability to control the channel number and geometry can be used to optimize the release of each type of macromolecule according to their own shape, size, and diffusive properties.

Drug release rates are shown to be tunable by changing channel number in Fig. 3G. Key to this implant technology is its ability to avoid burst release, release decay and dose dumping that are common to conventional polymeric drug eluting systems. The ideal release kinetics for intratumoral drug delivery is likely dependent on the type of immunomodulatory agent and its effect on TIME. Further, changes in TIME are associated with either negative or positive feedback loops in the immune response. Within this context, constant drug delivery allows for analyzing the impact of immunomodulatory agents on TIME without the confounding effects of variable dosing.

In vivo intratumoral NDES implantation and drug release

4T1 tumor-bearing mice were intratumorally implanted with the NDES using a one-time minimally invasive trocar approach. We leveraged the radiopacity of the implant to confirm implant placement within the tumor via CT scan (Fig. 4A). To evaluate the simultaneous release of two therapeutic antibodies via NDES in vivo, we used Alexa Fluor 647 and Alexa Fluor 790 to label agonist CD40 and anti-PDL1 antibodies, respectively (Fig. 4B-D). Fluorescence labeling permits in vivo drug tracking using IVIS live animal imaging. Fluorescently labeled antibodies were loaded into the NDES, which were then intratumorally implanted in 4T1-tumor bearing mice. We observed sustained intratumoral presence of CD40-AF647 and PDL1-AF790 in the tumor over 14 days (Fig. 4B-E). In our previous study, we showed that simultaneous intratumoral release of agonist CD40 and anti-PDL1 antibodies in conjunction with radiotherapy successfully reduced 4T1 tumor burden without causing toxicities associated with systemic treatment [17].

NDES delivered CD40/PDL1 antibodies treats EMT6 tumor

To assess treatment efficacy of NDES, we used the EMT6 orthotopic, syngeneic murine model of TNBC (Fig. 5A). The tumors were radiated daily using 5 Gy over 3 consecutive days, followed by intratumoral implantation of NDES containing CD40/PDL1 antibodies. The mice were monitored over 18 days post-NDES implantation. Body weight of the mice showed a drop soon after treatment, however they recovered after day 5 (Fig. 5B). Although NDES CD40/PDL1 demonstrated similar efficacy as radiation treatment alone in comparison to control untreated ($P<0.0001$; Fig. 5C), intratumoral treatment yielded tumor clearance in 3 out of 8 mice (Fig. 5D). Compared to NDES CD40/PDL1 only, the addition of radiation to NDES CD40/PDL1 markedly inhibited tumor growth ($P<0.01$), suggesting synergistic efficacy of combination treatment. In fact, combination treatment resulted in smaller tumors than baseline in 2 mice and 1 mouse had complete tumor clearance (Fig. 5C, D).

To assess the systemic immune activation potential of NDES treatment, we used a bilateral EMT6 tumor model to mimic primary tumor and metastasized distant tumor. In this study, only the left 'primary' tumors were treated via NDES CD40/PDL1, Rad only or Rad + NDES CD40/PDL1, and right 'distant' tumors were left untreated. Treatment response was assessed in both primary and distant tumors (Fig. 5E-H). Although NDES CD40/PDL1 did not reduce distant tumor burden, 1 out of 10 mice had complete elimination of the primary tumor (Fig. 5F). For Rad + NDES CD40/PDL1, 1 out of 8 mice showed complete tumor

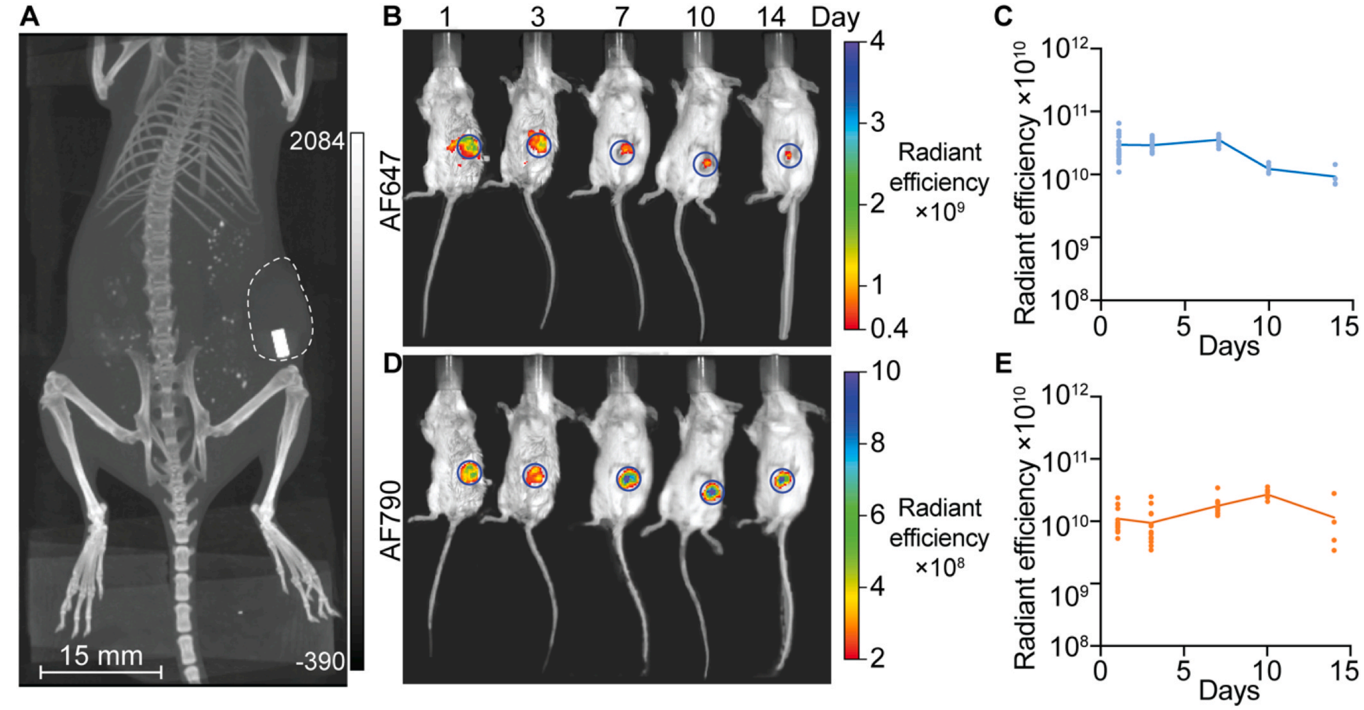

Fig. 4. CT scan to visualize intratumoral implant placement and IVIS imaging analysis for in vivo release of NDES containing agonist CD40-AF647 and anti-PDL1-AF790. A) CT scan of NDES intratumoral implant in 4T1 tumor-bearing mouse. B) IVIS images of 4T1 tumor bearing mice showing agonist CD40-AF647 across 14 days. C) ROI quantification of AF647 fluorescence signal. D) IVIS images of 4T1 tumor bearing mice showing anti-PDL1-AF790 across 14 days. E) ROI quantification of AF790 fluorescence signal.

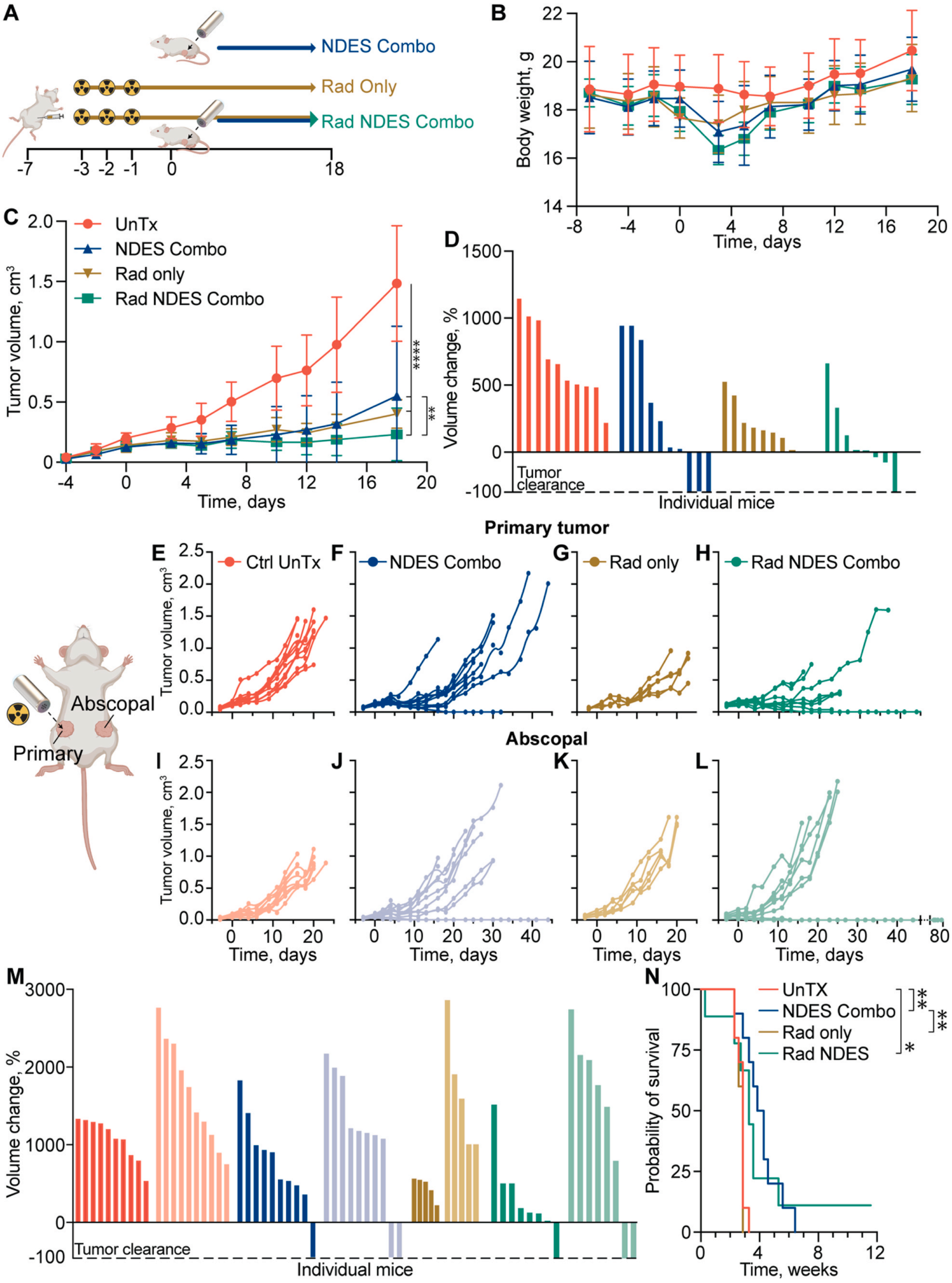

(caption on next page)

Fig. 5. NDES delivered CD40/PDL1 antibodies in EMT6 tumor-bearing mice. A) Treatment schematic of EMT6 mice depicting 5 Gy radiation therapy (Rad) pre-treatment for 3 consecutive days followed by CD40/PDL1 administration via NDES. B) Mice body weight over treatment period. C) Tumor volume of EMT6 mice: control untreated (UnTx), NDES CD40/PDL1, Rad only, Rad + NDES CD40/PDL1. Data are expressed as mean ± standard deviation (n=7/8 mice/group). Significance was analyzed by 2-way analysis of variance (ANOVA) ** > P.01, ****> P.0001. D) Tumor growth percentage of UnTx, NDES CD40/PDL1, Rad only, Rad + NDES CD40/PDL1. Each bar represents an individual mouse. Horizontal dashed line (-100%) indicates complete tumor clearance. E-L) Tumor growth curve of bilateral EMT6 tumor model to assess abscopal response, where only left tumors were treated. M) Tumor growth percentage UnTx, NDES CD40/PDL1, Rad only, Rad + NDES CD40/PDL1 in the bilateral tumor model. Each bar represents an individual mouse. Horizontal dashed line (-100%) indicates complete tumor clearance. N) Kaplan-Meier curves comparing progression- free survival of bilateral EMT6 tumor-bearing mice (log-rank Mantel-Cox test; n = 7–8/ group; *P <0.05, **P <0.01).

clearance up to day 44 (Fig. 5H). Thereafter, tumor recurred in the primary site, which was eliminated by day 67 time point. This mouse remained tumor free up until end of the experiment on day 81. In the bilateral tumor cohorts, Kaplan Meier analysis showed that Rad + NDES CD40/PDL1 had prolonged survival over control untreated, rad only and NDES CD40/PDL1 (Fig. 5I). On the same note, NDES CD40/PDL1 treatment improved survival over rad only group. Overall, these results showed the potential for local treatment to induce an abscopal response toward eliminating distant tumor lesions.

NDES delivered poly-STING agonist or poly-R848 treats 4T1 tumor

In a separate study, we demonstrated the tumor-treating capacity of NDES delivered STING agonist or R848 in 4T1 orthotopic, syngeneic murine model of TNBC (Fig. 6A-F). 4T1 tumors were intratumorally implanted with NDES containing either poly-STING agonist or poly-R848 in a one-time minimally invasive trocar approach. We noted no significant change in body weight compared to untreated control (Fig. 6B). For temperature, all mice across the groups showed normal fluctuations, with the exception of NDES PBS on day 5, which recovered thereafter (Fig. 6C). We noted that while 4T1 tumors responded to treatment, NDES poly-STING showed greater inhibition over poly-R848 under these release conditions (Fig. 6D-E).

Conclusions

Considering that current intratumoral immunotherapy delivery methods rely primarily on direct bolus injection, which rapidly disseminates from the tumor, it is challenging to discern the optimal dosing. Here we present an implant platform that sustainably releases drugs intratumorally, allowing for tumor exposure to a constant controlled dosing of immunotherapeutics. This could enable optimization of intratumoral immunotherapy regimens.

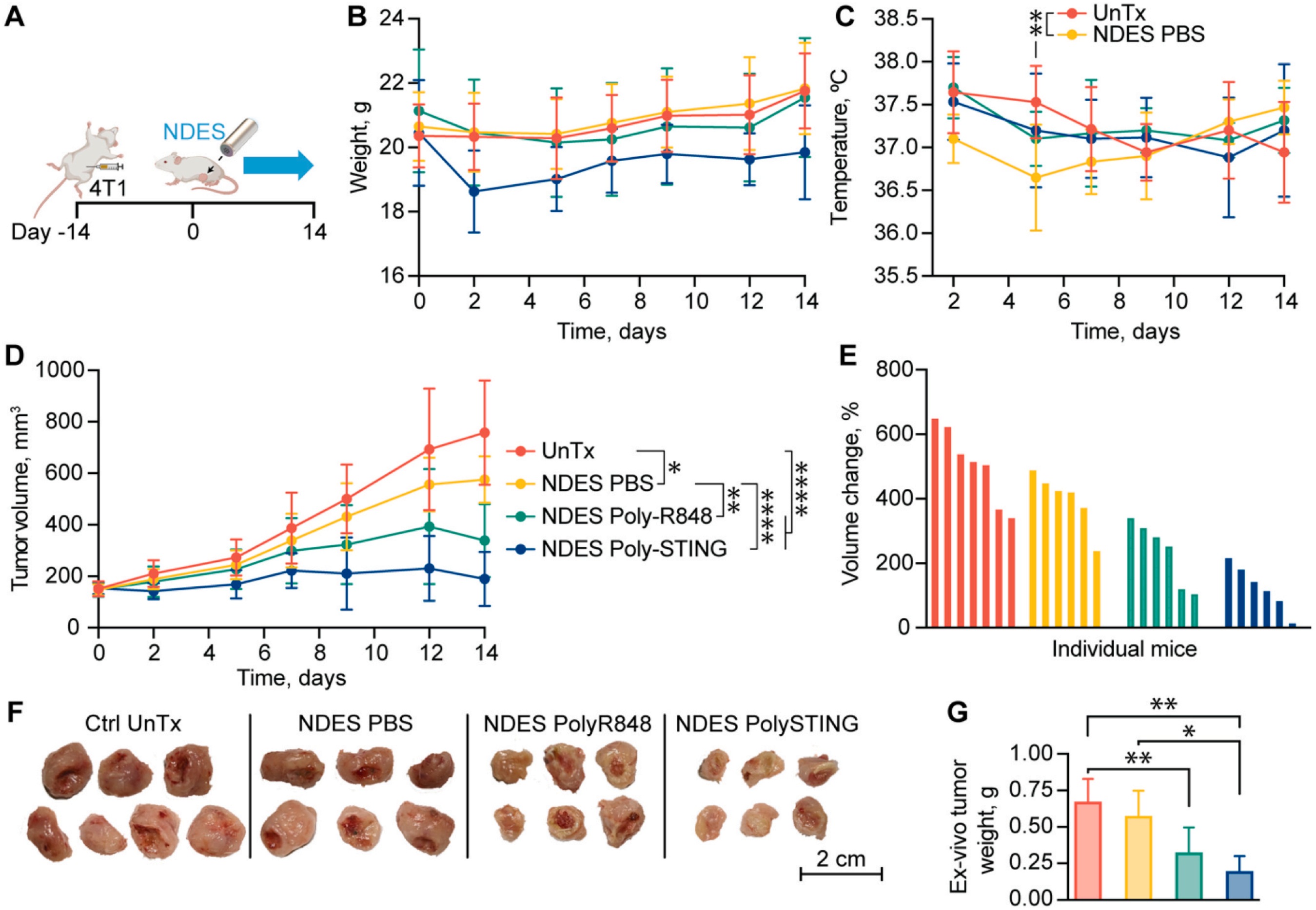

Fig. 6. NDES delivered poly-STING agonist or poly-R848 in 4T1 tumor-bearing mice. A) Treatment schematic of 4T1 mice. B) Mice body weight and C) temperature over treatment period. Significance was analyzed by 2-way ANOVA, ** < P 0.01. D) Tumor volume of 4T1 mice: control untreated (UnTx), NDES PBS, NDES Poly-R848, and NDES Poly-STING. Data are expressed as mean ± standard deviation (n=6–7 mice/group). Significance was analyzed by 2-way ANOVA, * P<0.05, ** P<0.01, **** P<0.0001. Ex vivo tumor E) images and F) weights. Significance was analyzed by one-way ANOVA, * P<0.05, ** P<0.01.

Funding

Funding support was received from the Houston Methodist Research Institute (A.G., C.Y.X.C.), Department of Defense (W81XWH-20–1–0600; A.G., S-H. C.), Nancy Owens Breast Cancer Foundation (C.Y. X.C.), Golfers Against Cancer (A.G., C.Y.X.C.), NIH-NCI R01CA257563 (P.S.), NIH-NIAID R01AI134729 (A.G., P.S.), the development of the nanochannel membrane was funded by NIH-NIGMS R01GM127558 (A. G.). Additional support was received through the Frank J. and Jean Raymond Centennial Chair Endowment.

CRediT authorship contribution statement

Patrick S. Stayton: Writing – review & editing, Validation, Supervision, Resources, Project administration, Methodology, Funding acquisition, Conceptualization. **Corrine Ying Xuan Chua:** Project administration, Funding acquisition, Conceptualization, Resources, Supervision, Validation, Writing – original draft, Writing – review & editing. **Abe Wu:** Investigation. **Alessandro Grattoni:** Conceptualization, Funding acquisition, Project administration, Resources, Supervision, Validation, Writing – original draft, Writing – review & editing. **Robin Vander Pol:** Investigation. **Ashley L. Joubert:** Investigation. **Ilaria Facchi:** Investigation. **Anthony M. Wood:** Investigation. **Jeremy Ho:** Investigation. **Federica Pesaresi:** Investigation. **Hsuan-Chen Liu:** Conceptualization, Data curation, Formal analysis, Investigation, Methodology, Software. **Valentina Cauda:** Supervision. **Nicola Di Trani:** Conceptualization, Data curation, Formal analysis, Investigation, Methodology, Software, Visualization, Writing – original draft, Writing – review & editing. **Shu-Hsia Chen:** Funding acquisition. **Marzia Conte:** Investigation. **Xuewu Liu:** Resources, Methodology, Funding acquisition, Conceptualization. **Đình Chương Nguyễn:** Investigation. **Simbarashe Jokonya:** Investigation.

Declaration of Competing Interest

The authors declare the following financial interests/personal relationships which may be considered as potential competing interests: Alessandro Grattoni and Shu-Hsia Chen reports financial support was provided by US Department of Defense. Corrine Ying Xuan Chua reports financial support was provided by Nancy Owens Breast Cancer Foundation. Corrine Ying Xuan Chua, Alessandro Grattoni reports financial support was provided by Golfers Against Cancer. Patrick S. Stayton reports financial support was provided by National Cancer Institute. Patrick S. Stayton, Alessandro Grattoni reports financial support was provided by National Institute of Allergy and Infectious Diseases. Alessandro Grattoni reports financial support was provided by National Institute of General Medical Sciences. Alessandro Grattoni has patent licensed to Semper Therapeutics.

Data Availability

Data will be made available on request.

Acknowledgments

We thank Dr. Jianhua (James) Gu from the electron microscopy core of Houston Methodist Research Institute.

Appendix A. Supporting information

Supplementary data associated with this article can be found in the online version at doi:10.1016/j.nantod.2024.102258.

References

[1] N. Momin, J.R. Palmeri, E.A. Lutz, N. Jailkhani, H. Mak, A. Tabet, M.M. Chinn, B. H. Kang, V. Spanoudaki, R.O. Hynes, K.D. Wittrup, Nat. Commun. 13 (2022) 109.

[2] T. Tang, X. Huang, G. Zhang, Z. Hong, X. Bai, T. Liang, Signal Transduct. Target. Ther. 6 (2021) 72.

[3] M. Binnewies, E.W. Roberts, K. Kersten, V. Chan, D.F. Fearon, M. Merad, L. M. Coussens, D.I. Gabrilovich, S. Ostrand-Rosenberg, C.C. Hedrick, R. H. Vonderheide, M.J. Pittet, R.K. Jain, W. Zou, T.K. Howcroft, E.C. Woodhouse, R. A. Weinberg, M.F. Krummel, Nat. Med. 24 (2018) 541–550.

[4] M. Binnewies, E.W. Roberts, K. Kersten, V. Chan, D.F. Fearon, M. Merad, L. M. Coussens, D.I. Gabrilovich, S. Ostrand-Rosenberg, C.C. Hedrick, R. H. Vonderheide, M.J. Pittet, R.K. Jain, W. Zou, T.K. Howcroft, E.C. Woodhouse, R. A. Weinberg, M.F. Krummel, Nat. Med. 24 (2018) 541–550.

[5] L. Xu, C. Zou, S. Zhang, T.S.M. Chu, Y. Zhang, W. Chen, C. Zhao, L. Yang, Z. Xu, S. Dong, H. Yu, B. Li, X. Guan, Y. Hou, F.-M. Kong, J. Hematol. Oncol. 15 (2022) 87.

[6] I. Melero, E. Castanon, M. Alvarez, S. Champiat, A. Marabelle, Nat. Rev. Clin. Oncol. 18 (2021) 558–576.

[7] J. Humeau, J. Le Naour, L. Galluzzi, G. Kroemer, J.G. Pol, Oncoimmunology 10 (2021) 1984677.

[8] M. Ghosn, L. Tselikas, S. Champiat, F. Deschamps, B. Bonnet, É. Carre, M. Testan, F. X. Danlos, S. Farhane, S. Susini, S. Suzzoni, S. Ammari, A. Marabelle, T. De Baere, Curr. Oncol. Rep. 25 (2023) 857–867.

[9] S. Champiat, L. Tselikas, S. Farhane, T. Raoult, M. Texier, E. Lanoy, C. Massard, C. Robert, S. Ammari, T. De Baère, A. Marabelle, Clin. Cancer Res. 27 (2021) 665–679.

[10] M.A. Aznar, N. Tinari, A.J. Rullán, A.R. Sánchez-Paulete, M.E. Rodriguez-Ruiz, I. Melero, J. Immunol. 198 (2017) 31–39.

[11] W.X. Hong, S. Haebe, A.S. Lee, C.B. Westphalen, J.A. Norton, W. Jiang, R. Levy, Clin. Cancer Res. 26 (2020) 3091–3099.

[12] A. Som, J.G. Rosenboom, A. Chandler, R.A. Sheth, E. Wehrenberg-Klee, Adv. Drug Deliv. Rev. 189 (2022) 114505.

[13] N.M. Muñoz, M. Williams, K. Dixon, C. Dupuis, A. McWatters, R. Avritscher, S. Z. Manrique, K. McHugh, R. Murthy, A. Tam, A. Naing, S.P. Patel, D. Leach, J. D. Hartgerink, S. Young, P. Prakash, P. Hwu, R.A. Sheth, J. Immunother. Cancer 9 (2021).

[14] C.Y.X. Chua, J.S. Ho, S. Demaria, M. Ferrari, A. Grattoni, Adv. Ther. (2020).

[15] C.Y.X. Chua, P. Jain, A. Susnjar, J. Rhudy, M. Folci, A. Ballerini, A. Gilbert, S. Singh, G. Bruno, C.S. Filgueira, C. Yee, E.B. Butler, A. Grattoni, J. Control. Release 285 (2018) 23–34.

[16] H.C. Liu, D. Davila Gonzalez, D.I. Viswanath, R.S. Vander Pol, S.Z. Saunders, N. Di Trani, Y. Xu, J. Zheng, S.H. Chen, C.Y.X. Chua, A. Grattoni, Adv. Sci. 10 (2023) e2206873.

[17] H.C. Liu, D.I. Viswanath, F. Pesaresi, Y. Xu, L. Zhang, N. Di Trani, J. Paez-Mayorga, N. Hernandez, Y. Wang, D.R. Erm, J. Ho, A. Susnjar, X. Liu, S. Demaria, S.H. Chen, B.S. Teh, E.B. Butler, C.Y. Xuan Chua, A. Grattoni, Int. J. Radiat. Oncol. Biol. Phys. 110 (2021) 492–506.

[18] G. Bruno, N. Di Trani, R.L. Hood, E. Zabre, C.S. Filgueira, G. Canavese, P. Jain, Z. Smith, D. Demarchi, S. Hosali, A. Pimpinelli, M. Ferrari, A. Grattoni, Nat. Commun. 9 (2018) 1682.

[19] N. Di Trani, A. Pimpinelli, A. Grattoni, ACS Appl. Mater. Interfaces 12 (2020) 12246–12255.

[20] S. Ferrati, D. Fine, J. You, E. De Rosa, L. Hudson, E. Zabre, S. Hosali, L. Zhang, C. Hickman, S. Sunder Bansal, A.M. Cordero-Reyes, T. Geninatti, J. Sih, R. Goodall, G. Palapattu, M. Kloc, R.M. Ghobrial, M. Ferrari, A. Grattoni, J. Control Release 172 (2013) 1011–1019.

[21] D. Fine, A. Grattoni, S. Hosali, A. Ziemys, E. De Rosa, J. Gill, R. Medema, L. Hudson, M. Kojic, M. Milosevic, L. Brousseau Iii, R. Goodall, M. Ferrari, X. Liu, Lab Chip 10 (2010) 3074–3083.

[22] Y. Zhu, X. An, X. Zhang, Y. Qiao, T. Zheng, X. Li, Mol. Cancer 18 (2019) 152.

[23] R.L. Sabado, A. Pavlick, S. Gnjatic, C.M. Cruz, I. Vengco, F. Hasan, M. Spadaccia, F. Darvishian, L. Chiriboga, R.M. Holman, J. Escalon, C. Muren, C. Escano, E. Yepes, D. Sharpe, J.P. Vasilakos, L. Rolnitzsky, J. Goldberg, J. Mandeli, S. Adams, A. Jungbluth, L. Pan, R. Venhaus, P.A. Ott, N. Bhardwaj, Cancer Immunol. Res. 3 (2015) 278–287.

[24] R.H. Vonderheide, Annu. Rev. Med. 71 (2020) 47–58.

[25] J. Gong, A. Chehrazi-Raffle, S. Reddi, R. Salgia, J. Immunother. Cancer 6 (2018) 8.

[26] H.-C. Liu, D.I. Viswanath, F. Pesaresi, Y. Xu, L. Zhang, N. Di Trani, J. Paez-Mayorga, N. Hernandez, Y. Wang, D.R. Erm, J. Ho, A. Susnjar, X. Liu, S. Demaria, S.-H. Chen, B.S. Teh, E.B. Butler, C.Y. Xuan Chua, A. Grattoni, Int. J. Radiat. Oncol. Biol. Phys. (2020).

[27] H.C. Liu, D. Davila Gonzalez, D.I. Viswanath, R.S. Vander Pol, S.Z. Saunders, N. Di Trani, Y. Xu, J. Zheng, S.H. Chen, C.Y.X. Chua, Adv. Sci. 10 (2023) 2206873.

[28] T. Geninatti, E. Small, A. Grattoni, Meas. Sci. Technol. 25 (2014) 027003.

[29] G. Scorrano, G. Bruno, N. Di Trani, M. Ferrari, A. Pimpinelli, A. Grattoni, ACS Appl. Mater. Interfaces 10 (2018) 32233–32238.

[30] H. Hackstein, A. Knoche, A. Nockher, J. Poeling, T. Kubin, M. Jurk, J. Vollmer, G. Bein, Cell. Immunol. 271 (2011) 401–412.

[31] S. Tambunlertchai, S.M. Geary, A.K. Salem, Pharmaceutics 14 (2022) 2076.

[32] J.M. Ramanjulu, G.S. Pesiridis, J. Yang, N. Concha, R. Singhaus, S.-Y. Zhang, J.-L. Tran, P. Moore, S. Lehmann, H.C. Eberl, Nature 564 (2018) 439–443.

[33] F.-Y. Su, S. Srinivasan, B. Lee, J. Chen, A.J. Convertine, T.E. West, D.M. Ratner, S. J. Skerrett, P.S. Stayton, J. Control. Release 287 (2018) 1–11.

[34] J. Chen, F.-Y. Su, D. Das, S. Srinivasan, H.-N. Son, B. Lee, F. Radella II, D. Whittington, T. Monroe-Jones, T.E. West, Biomaterials 195 (2019) 38–50.

[35] T.E. Chavas, F.-Y. Su, S. Srinivasan, D. Roy, B. Lee, L. Lovelace-Macon, G.F. Rerolle, E. Limqueco, S.J. Skerrett, D.M. Ratner, J. Control. Release 330 (2021) 284–292.

[36] S. Lv, K. Song, A. Yen, D.J. Peeler, D.C. Nguyen, A. Olshefsky, M. Sylvestre, S. Srinivasan, P.S. Stayton, S.H. Pun, Adv. Healthc. Mater. 11 (2022) 2101651.

[37] K. Song, D.C. Nguyen, T. Luu, O. Yazdani, D. Roy, P.S. Stayton, S.H. Pun, J. Control. Release 356 (2023) 232–241.

[38] D.S. Wilson, S. Hirosue, M.M. Raczy, L. Bonilla-Ramirez, L. Jeanbart, R. Wang, M. Kwissa, J.-F. Franetich, M.A. Broggi, G. Diaceri, Nat. Mater. 18 (2019) 175–185.

[39] J. De Mel, M. Hossain, O. Shofolawe-Bakare, S.A. Mohammad, E. Rasmussen, K. Milloy, M. Shields, E.W. Roth, K. Arora, R. Cueto, Mol. Pharm. 19 (2022) 4705–4716.

[40] G. Bruno, N. Di Trani, R.L. Hood, E. Zabre, C.S. Filgueira, G. Canavese, P. Jain, Z. Smith, D. Demarchi, S. Hosali, A. Pimpinelli, M. Ferrari, A. Grattoni, Nat. Commun. 9 (2018) 1682.

[41] N. Di Trani, A. Pimpinelli, A. Grattoni, ACS Appl. Mater. Interfaces 12 (2020) 12246–12255.

[42] N. Di Trani, N. Racca, D. Demarchi, A. Grattoni, ACS Appl. Mater. Interfaces, (2022).

[43] N. Di Trani, A. Silvestri, Y. Wang, D. Demarchi, X. Liu, A. Grattoni, Pharmaceutics 12 (2020) 679.